Wind Signatures in the X-ray Emission Line Profiles of the Late O Supergiant ζ Orionis

David H. Cohen[1], Maurice A. Leutenegger[2], Kevin Grizzard[1,3], Catherine Reed[1], Roban H. Kramer[1,2,4], Stanley P. Owocki[5]

cohen@astro.swarthmore.edu; maurice@astro.columbia.edu; kevin.grizzard@sjca.edu; caseyreed@alum.swarthmore.edu; roban@astro.columbia.edu; owocki@bartol.udel.edu

ABSTRACT

X-ray line profile analysis has proved to be the most direct diagnostic of the kinematics and spatial distribution of the very hot plasma around O stars. The Doppler-broadened line profiles provide information about the velocity distribution of the hot plasma, while the wavelength-dependent attenuation across a line profile provides information about the absorption to the hot plasma, thus providing a strong constraint on its physical location. In this paper we apply several analysis techniques to the *Chandra* HETGS spectrum of the late-O supergiant ζ Ori (O9.7 Ib), including the fitting of a simple line-profile model. We show that there is distinct evidence for blue shifts and profile asymmetry, as well as broadening in the X-ray emission lines of ζ Ori. These are the observational hallmarks of a wind-shock X-ray source, and the results for ζ Ori are very similar to those for the earlier O star, ζ Pup, which we have previously shown to be well-fit by the same wind-shock line-profile model. The more subtle effects on the line-profile morphologies in ζ Ori, as compared to ζ Pup, are consistent with the somewhat lower density wind in this later O supergiant. In the context of the recent reanalysis of the helium-like line intensity ratios in this star, and also in light of recent work questioning the accepted mass-loss rates in OB stars, these new results indicate that the X-ray emission from ζ Ori can be understood within the framework of the standard wind-shock scenario for hot stars.

[1]Swarthmore College Department of Physics and Astronomy, 500 College Ave., Swarthmore PA 19081

[2]Columbia University, Department of Physics and Columbia Astrophysics Laboratory, 550 W. 120$^{\rm th}$ St., New York NY 10027

[3]St. John's College, 60 College Ave., Annapolis MD 21401

[4]Prism Computational Sciences, 455 Science Dr., Suite 140, Madison WI 53711

[5]Bartol Research Institute, University of Delaware, 217 Sharp Laboratory, Newark DE 19716

Subject headings: line: profiles — stars: early-type — stars: mass loss — stars: winds, outflow — stars: individual (ζ Ori) — X-rays: stars

1. Introduction

X-ray emission from normal, single OB stars has generally been explained in terms of shock heating of the massive, highly supersonic, radiation-driven winds of these very luminous stars (Pallavicini, et al. 1981; Corcoran et al. 1993; Hillier et al. 1993; Cassinelli et al. 1994; Drew, Hoare, & Denby 1994; Cohen et al. 1996; Kudritzki et al. 1996; Owocki & Cohen 1999). The standard model involves the line-force instability, initially noted in the context of hot star winds by Lucy & Solomon (1970) and later investigated by Lucy & White (1980); Lucy (1982); Owocki & Rybicki (1984); Owocki, Castor, & Rybicki (1988); Feldmeier et al. (1997); Feldmeier, Puls, & Pauldrach (1997); Runacres & Owocki (2002). Other wind-shock models of X-ray production have also been discussed, based on co-rotating interaction regions (Mullan 1984), driven shocks (MacFarlane & Cassinelli 1989), and inverse Compton scattering (Chen & White 1991). Even in the context of the line-force instability mechanism, there are different scenarios based on the self-excited instability (Owocki, Castor, & Rybicki 1988) versus the instability seeded by perturbations at the base of the wind (Feldmeier et al. 1997), and one-dimensional simulations versus two-dimensional simulations (Dessart & Owocki 2003).

Despite this proliferation of models, very few observational constraints could be put on any of these wind-shock models. This was at least partly because of the very limited data quality of X-ray observations before the late 1990s. Furthermore, the idea that dynamo-driven coronal mechanisms, similar to what is seen on the Sun, might be relevant to hot-star X-ray production, continues to have adherents (Cassinelli & Olson 1979; Waldron 1984; Smith et al. 1993; Waldron & Cassinelli 2001; Smith et al. 2004). Finally, it has recently been suggested that a hybrid wind-magnetic shock-heating X-ray production mechanism is in operation on at least some hot stars (Gagné et al. 1997; Babel & Montmerle 1997a,b; ud-Doula & Owocki 2002; Schulz et al. 2003; Gagné et al. 2005).

The launch of the *Chandra* and *XMM* telescopes in 1999, with their high-resolution grating spectrometers, vastly improved the quality of X-ray spectra available from OB stars. Although these missions provided a huge increase in the amount of information in the X-ray data, they have not led to a consensus in the community regarding the actual X-ray production mechanism in hot stars. This is partly because of the diverse behavior seen in the half-dozen or so normal (not interacting binary) hot stars thus far observed. And it is also partly due to the lack of connection between the diagnostics usually employed in the

analysis of grating spectra of O stars and any quantitative physical model.

The high resolution of the new X-ray grating spectrometers provides a powerful diagnostic of plasma kinematics and location (via the effects of continuum absorption), and thus potentially a discriminant among the various physical models, in the form of resolved emission line profiles. Hot plasma embedded in a fast stellar wind should produce Doppler broadened emission lines, with the velocity and density structure dictating the detailed form of these profiles. Continuum absorption by the bulk, unshocked wind will be stronger on the red wing of an emission line, as the photons emitted from the back side of the wind are seen through a larger column of material than those emitted from the front, blue shifted side. Overall, then, a wind-shock mechanism, in which the shock-heated plasma is embedded in a more-or-less spherically symmetric cold wind, should lead to blue shifted, asymmetric lines with a characteristic shape (MacFarlane et al. 1991; Ignace 2001; Owocki & Cohen 2001).

The diverse behavior observed in the first hot stars observed with *Chandra* and *XMM* includes line profiles that are broad, shifted, and skewed in the earliest O stars (Kahn et al. 2001; Cassinelli et al. 2001) but are quite narrow in early B stars (Cohen et al. 2003; Mewe et al. 2003) and young O stars (Schulz et al. 2003; Gagné et al. 2005), with the X-ray emission lines of late O supergiants having a more intermediate morphology (Waldron & Cassinelli 2001; Miller et al. 2002).

The O4 star ζ Pup seems to be generally accepted as fitting the wind-shock paradigm, based on its line profiles. The broad, shifted, and asymmetric profiles are qualitatively what is expected from a spherically symmetric wind source (Cassinelli et al. 2001). Quantitative analysis (Kramer, Cohen, & Owocki 2003) shows that the hot plasma is distributed throughout the wind above some minimum radius of emission that is approximately half a stellar radius above the photosphere; that it is distributed roughly as the density-squared of the bulk wind; and that the kinematics of the hot plasma are consistent with the underlying beta-velocity law of the bulk wind. This same analysis does, however, show that there is significantly less continuum absorption than would be expected for a smooth, spherically symmetric wind having a mass-loss rate consistent with UV and H_α observations and wind opacity consistent with models. This might be explained by a reduction in the mass-loss rate or by inhomogeneities in the wind ("porosity" or "clumping"). To the extent that the wind-shock picture is applicable to ζ Pup, it has generally been supposed, however, that this very early O star is the only hot star for which the standard wind-shock scenario can explain the *Chandra* observations.

Meanwhile, the late-O supergiant ζ Ori has X-ray lines that are broad enough to be understood in the context of the wind-shock scenario (Waldron & Cassinelli 2001). These authors, however, reported that there was no systematic trend in the Doppler shifts of the emis-

sion lines observed with *Chandra*, and additionally, that the forbidden-to-intercombination line ratio of Si XIII indicates a location so close to the photosphere that it could not be explained in the context of wind-shock models. However, no quantitative assessment has yet been made of the line profile shapes. In this paper we quantitatively examine the shift and asymmetry in the X-ray emission lines on ζ Ori. We do this first by fitting Gaussians to the strong emission lines in the *Chandra* spectrum, and then by performing a non-parametric analysis of the line shift and asymmetry, and finally by applying the simple line-profile model that was successfully used to fit the X-ray emission lines in the *Chandra* spectrum of ζ Pup. We show that the X-ray emission lines in ζ Ori actually can be as well fit by standard wind-shock models as those in ζ Pup, with a similar finding of lower-than-expected wind absorption. We also discuss the results of our line-profile analysis of ζ Ori in light of a reevaluation of the forbidden-to-intercombination line ratios that revises the earlier results to show no significant conflict with a wind-shock origin for the X-rays (Leutenegger et al. 2006).

In §2 we briefly describe the observational data and the properties of ζ Ori. In §3 we assess the blue shifts and skewness of the line profiles quantitatively but in a non-model-dependent way. In §4 we fit an analytic, spherically symmetric wind emission and absorption line-profile model (Owocki & Cohen 2001) to eleven lines in the *Chandra* spectrum of ζ Ori. In §5 we discuss the results of the model fitting and their interpretation, including how these results comport with other X-ray diagnostics, especially the helium-like forbidden-to-intercombination line flux ratios. Finally, we summarize our conclusions in §6.

2. The *Chandra* Data and Stellar Properties

The data analyzed in this paper was obtained during the *Chandra* AO1 GO phase, using the ACIS-S/HETGS configuration, and made with nominal pointing at ζ Ori. The effective exposure time was 73.87 ks, with the data comprising two Obs. IDs: 610 and 1524, taken on 8 April 2000 and 9 April 2000, respectively. In the combined data, 11,347 first order MEG counts were recorded. The dispersed spectrum is quite soft, as can be seen in Figure 1, and there were significantly more counts in the MEG than in the HEG spectrum, which had only 2508 total first-order counts. We therefore used only the MEG spectrum for the line profile analysis in this paper. We performed the standard reduction and extraction of the dispersed spectra using the basic grating threads and CIAO v3.1 and CALDB v2.28. We checked the centroids of strong lines separately in the negative and positive first order spectra and did not see any significant systematic shift in the wavelengths of the emission lines between the negative and positive sides. We wrote the count spectra (-1 and +1 orders) to ascii

files, and performed the analysis with custom-written codes in IDL and *Mathematica*, except for the initial fitting of Gaussian line profiles, which we performed within CIAO/Sherpa. We then repeated the fits of wind-profile models to individual lines using a custom written model within *XSPEC* v11.3.1. For the *XSPEC* fitting, we used only Obs. ID 610 (exposure time of 59.63 ks), as including the second, much shorter, Obs. ID did not improve the statistics on the fits at all. For all the model fitting we performed, we used the C statistic to assess the goodness-of-fit and parameter confidence limits, as the data in the line wings and nearby continuum has a small number of counts per bin (Cash 1979). We discuss the fitting procedure in detail in §4.

The late O supergiant, ζ Ori (Alnitak, HD37742, the eastern-most of the Orion belt stars), has a spectral classification of O9.7 and a luminosity class Ib (Maíz-Apellániz et al. 2004), and as such is significantly cooler than the O4 prototype ζ Pup, which shows X-ray emission line profiles consistent with the wind-shock scenario. The wind mass-loss rate determinations for ζ Ori are roughly a factor of two lower than those for ζ Pup. The Hipparcos distance is 277^{+73}_{-49} pc (Perryman et al. 1997). Other important stellar and wind parameters taken from the literature are listed in Table 1. The overall X-ray properties of ζ Ori are quite typical of O stars ($kT_{\rm X} \leq 1$ keV, $L_{\rm X}/L_{\rm Bol} \approx 10^{-7}$), although it is one of the few O stars to have shown any significant time variability (Berghofer & Schmitt 1994). There is no evidence for variability in the *Chandra* data.

3. Phenomenological and Non-Parametric Analysis of the Line Profiles

The simplest method, and a common mode, of examining hot-star emission line properties is the fitting of Gaussian line-profile models. These are convolved with the instrumental response function and multiplied by the instrument effective area and fit to individual lines allowing for an assessment of the centroid shifts, line widths, and amplitudes. Indeed, this approach was taken in the discovery paper for ζ Ori (Waldron & Cassinelli 2001). Waldron & Cassinelli (2001) reported significant broadening (velocity dispersion of 900 ± 200 km s^{-1}), but also noted the generally symmetric appearance of the lines and claimed a lack of any trend in line centroid shifts.

We recapitulate this simple approach here, but also quantitatively examine the quality of the Gaussian fits, including the distribution of the residuals. In Figure 2 we look at two of the strongest unblended lines in the spectrum, O VIII Ly$_\alpha$ at 18.97 Å and Fe XVII at 15.01 Å. In these fits, shown in the top panels of each column, the centroid of the Gaussian was fixed at the laboratory rest wavelength (the oscillator-strength-weighted mean of the two components of the Ly$_\alpha$ doublet in the case of the oxygen feature) and a power law was

fit simultaneously to the weak continuum. These fits are formally bad when analyzed using Monte Carlo simulations of the C statistic distribution - rejected at more than the 90% level. There are clear indications of line profile asymmetries in the residuals of the Gaussian fit, in the sense one would expect from a wind-shock model, with a blue-shifted peak and steeper blue wings and shallower red wings.

We next fit a Gaussian model with the centroid allowed to be a free parameter. This model (shown in the middle panel of each column in Figure 2) fits the line profile better, but there are clearly still systematic trends in the distribution of fit residuals. Again, the actual line profiles have blue wings that are steeper than the Gaussians and red wings that are shallower. The Monte Carlo analysis of the C statistic distributions shows that these fits are better than those with the fixed Gaussian centroids, having rejection probabilities of only 68% and 73%, for the O VIII and Fe XVII lines, respectively.

The widths and centroid shifts can be estimated from these Gaussian fits, even if the model is not ideal. For the oxygen Ly_α line, we find a best fit Gaussian (half width at half maximum) HWHM of 830 ± 50 km s^{-1}, and a centroid blue shift of -150 ± 30 km s^{-1}. Most other lines have even larger shifts, as can be seen in Table 2, in which we show the results of fits to nine emission lines in the spectrum. These values seem plausible in the context of the wind-shock scenario, although one might ask what values of the peak blue shifts and the HWHMs would be expected in this case. The estimated terminal velocity of the wind is, after all, twice the value of the derived HWHMs. The answer will depend on the spatial distribution of the X-ray emitting plasma, the velocity distribution, and the degree of attenuation (see Fig. 2 in Owocki & Cohen (2001)). We will show in the remainder of this section and the next one that there are quantitative indications of line asymmetries, even apart from the application of any specific wind model, and that an empirical wind model does in fact fit the line profiles better than the shifted Gaussian model (the wind-profile model is shown in the bottom two panels of Figure 2, but not discussed until §4). Although we cannot reject the shifted Gaussian model with a high degree of certainty for any one emission line in the spectrum of ζ Ori, the Gaussian fitting suggests some degree of line profile asymmetry and, more generally, that a more appropriate and physically meaningful model might improve the quality of the fits.

But before fitting wind-profile models, let us first characterize the line profile shapes using a model-independent, non-parametric analysis. We do this by computing the first three moments of the observed line profiles, describing respectively the centroid shift, width, and asymmetry of the line profiles, as computed from:

$$M_1 \equiv \frac{\sum_{i=1}^{N} x_i f(x_i)}{\sum_{i=1}^{N} f(x_i)}$$

$$M_2 \equiv \frac{\sum_{i=1}^{N} (x_i - M_1)^2 f(x_i)}{\sum_{i=1}^{N} f(x_i)}$$

$$M_3 \equiv \sum_{i=1}^{N} (x_i - M_1)^3 f(x_i).$$

Here x is a dimensionless wavelength variable scaled to the terminal velocity of the wind, with the laboratory rest wavelength of each line set to $x = 0$, as $x \equiv \frac{(\lambda - \lambda_o)}{\lambda} \frac{c}{v_\infty}$, and with $f(x_i)$, the number of counts in the i^{th} bin of N total bins at scaled wavelength x_i. Note that we have not normalized the third moment in our definition, in order to make the calculation of its formal uncertainty more straightforward. The standard definition of the skewness, s, is related to our definition of the third moment according to $s \equiv \frac{M_3}{M_2^3 \sum_{i=1}^{N} f(x_i)}$.

We propagate the formal uncertainties for each calculated moment from the Poisson errors on the total number of counts in each (scaled) wavelength bin. We note that we have not corrected for the instrumental broadening, which is quite symmetric, and not very large, compared to the observed line widths, and so will not affect the first and third moments significantly. We also have not corrected for the weak continuum present under each line or for the wavelength-dependence of the detector effective area. But both of these factors are explored in quantitative detail in the next section, and are shown generally to be negligible. We list the values of the first and third moments for the strong, unblended lines along with their formal uncertainties in Table 3. The second moments are not listed, although they are quite large, because we have already determined from the Gaussian fitting that the lines are broad and in the moment analysis we cannot separate out the effects of physical broadening from instrumental broadening. We use only the unblended lines in this analysis because the moment values have meaning only if they are calculated on a symmetric domain about $x = 0$. In all cases we use the domain $[-1 : 1]$ and assume a value of $v_\infty = 1860$ km s^{-1} for the wind terminal velocity. In Figure 3 we show two emission lines, with the moment-analysis domains indicated, along with the laboratory rest wavelengths and the values of the first moments.

The numerical values of the first moments are straightforward to interpret. They represent the position of each line centroid in units of x. The values of the third moments, however, are difficult to interpret by themselves. But their significance level in terms of formal uncertainties (i.e. their "sigma" levels, listed in the final column of Table 3) are the

relevant quantity for assessing whether each line has a non-zero skewness (asymmetry) that is statistically significant. Unshifted and symmetric lines should have first and third moments that are consistent with zero. The emission lines analyzed for ζ Ori are significantly blue shifted (negative first moments), which is consistent with the results of the Gaussian fitting, but which contradicts the assertion of Waldron & Cassinelli (2001) that there are no systematic red shifts or blue shifts in the emission lines. It is also clear from the moment analysis that the lines are significantly redward skewed (positive third moments), generally between the 1 and 2 sigma levels for each line. This asymmetry was not noted in the earlier analysis, which relied on "eyeballing" the Gaussian fits (Waldron & Cassinelli 2001). A redward skewness (along with the blue shifted centroids) is exactly what is expected from continuum absorption in the context of a fast, spherically symmetric stellar wind (Owocki & Cohen 2001). The redward skewness comes about from the steep blue wing and the more extended, shallower red wing.

4. Wind Profile Model Fits to the Emission Lines

In the previous section we showed that there is evidence for blue shifting, redward skewness, and broadening in the X-ray emission lines of the O supergiant ζ Ori. These results are consistent with the expectations of a generic wind-shock picture. To augment this model-independent characterization of the net profile shift and skewness, and to derive physical information about the applicability of a wind-shock model, let us next fit a simple, empirical wind-shock line-profile model to eleven relatively strong lines in the MEG spectrum of ζ Ori. We use the empirical wind-profile model of Owocki & Cohen (2001), which is physical, in the sense that it accounts for the Doppler shifted emission and radiation transport, including continuum attenuation, through a three-dimensional, spherically symmetric expanding wind. The parameters of the model have specific, physical meanings related to the spatial distribution of the hot plasma and the amount of absorption by the bulk, unshocked wind. The model is empirical, in that it does not posit any specific heating mechanism, and thus is applicable to a wide range of possible wind-shock (and even coronal) scenarios for X-ray emission.

The goal of fitting the wind-profile model is thus to constrain the physical parameters of the wind emission and absorption for each strong emission line in the *Chandra* spectrum of ζ Ori. Theorists may then compare the predictions of any number of specific models or numerical simulations to the physical parameter values we derive. Furthermore, our fitting of wind-profile models allows us to quantify the amount of asymmetry in the line profiles and relate the asymmetry, quantitatively, to the amount of wind absorption, through the

optical depth parameter of the wind-profile model,

$$\tau_* \equiv \frac{\kappa \dot{M}}{4\pi v_\infty \mathrm{R}_*},$$

where κ is the absorption opacity, and $\dot{M}$ is the mass-loss rate. Physically, τ_* represents the optical depth along a central ray from infinity to the stellar surface radius R_*, in the simplified case that the wind velocity is constant at the terminal value, v_∞. In this simplified, constant-velocity case, a value of $\tau_* > 1$ also represents the radius of unit optical depth, R_1, expressed in units of R_*. The wind-profile model assumes that the hot plasma is distributed throughout the wind, above some minimum radius, $R_{\rm min}$, and that its filling factor is proportional to the ambient wind density multiplied by an additional power-law factor, $f \propto r^{-q}$ (thus falling off as $1/vr^{(2+q)}$). The other two interesting parameters of the model are thus q and $R_{\rm min}/\mathrm{R}_*$ (sometimes expressed as $u_{max} \equiv \mathrm{R}_*/\mathrm{R}_{\rm min}$). The normalization of the profile is the fourth, and final, parameter. There is an implicit assumption that there are enough different regions of hot plasma that the wind can be treated as a two-component fluid, comprising a bulk, cool ($T \approx T_{\rm eff}$), X-ray absorbing component, with a hot, X-ray emitting component smoothly mixed in. The minimum radius of the hot plasma distribution is motivated by numerical simulations that show that large shocks tend not to form until the wind flow has reached at least several tenths of a stellar radius, in the context of self-excited instabilities (Cohen et al. 1996; Cooper 1996; Feldmeier et al. 1997).

As discussed in further detail in Owocki & Cohen (2001), the line profile is computed from the integral

$$L_{\rm x} \propto \int_{r=r_x}^{\infty} \frac{r^{-(q+2)}}{(1-\mathrm{R}_*/\mathrm{r})^{3\beta}} \exp[-\tau(\mu_x, r)] dr,$$

where $r_x \equiv \max[R_{\rm min}, \mathrm{R}_*/(1-|\mathrm{x}|^{1/\beta})]$, $\mu_x \equiv x/(1-\mathrm{R}_*/\mathrm{r})^\beta$, and $\tau(\mu, r)$ (which is proportional to τ_*) is the optical depth along the observer's line of sight at direction cos μ and radial coordinate r. Here the scaled wavelength, $x \equiv (\lambda/\lambda_o - 1)(c/v_\infty)$, is the same quantity we used in the moment analysis. The parameter β is the usual wind acceleration parameter, from $v = v_\infty(1-\mathrm{R}_*/\mathrm{r})^\beta$. The governing equation for $L_{\rm x}$ must be solved numerically for all $\beta \neq 0$. We set $\beta = 1$ in all of our fits. We include a power law continuum model in all the fits we performed in *XSPEC*. Finally, we note that this model implicitly assumes spherical symmetry and a smooth wind flow.

Again, this wind-profile model is both physically meaningful and widely applicable to a range of different physical models of X-ray production, including coronal models (see Fig. 2 in

Owocki & Cohen (2001) for a graphical exploration of the effects of choosing different model parameter values on the line profile shapes, and Fig. 4 in the same paper for a comparison of wind-shock and coronal model parameters). The larger $R_{\rm min}$ is and the smaller q is, the broader the line profiles tend to be. We note that for a wide range of realistic choices of these parameters, the characteristic width of the resulting profiles is equivalent to roughly half the terminal velocities, consistent with the half-widths we derived from the Gaussian fits in the previous section. The wind optical depth parameter, τ_*, tends to make the profiles more narrow, more blue shifted, and more asymmetric, as its value increases. A model with a relatively small $R_{\rm min}$ value and a negligible τ_* produces a profile that is similar in shape to a Gaussian.

We fit this wind-profile model to each strong line in the ζ Ori MEG spectrum, allowing all four adjustable parameters (q, $R_{\rm min}$, τ_*, and the normalization) to be free, in conjunction with a power-law component to model the weak continuum emission. For several lines, multiple profiles are fit simultaneously to account for blending. This included the helium-like resonance and intercombination lines of oxygen. We do not give fits to the other helium-like complexes in the ζ Ori *Chandra* spectrum, as fits to these complexes are reported elsewhere (Leutenegger et al. 2006). For the Fe XVII line at 16.78 Å we fit only the negative first order spectrum, as the positive first order spectrum had very few counts in this line.

As mentioned previously, we first carried out this modeling using the same procedure, implemented in *Mathematica*, that we employed in our earlier analysis of ζ Pup (Kramer, Cohen, & Owocki 2003). We then repeated the modeling using a custom-written module in *XSPEC*, which allowed us to include a continuum emission component in the modeling and use the exact instrumental responses. This also enabled us to simultaneously fit multiple models to line blends. The two methods gave very similar results. The results of the *XSPEC* model-fitting are summarized in Table 4, and the best-fit models, superimposed on the data, are shown in Figure 4. For the oxygen Ly$_\alpha$ line and the Fe XVII 15.01 Å line, the results are shown in the bottom row of panels in Figure 2. The wind-profile model does indeed provide better fits to most (ten out of eleven) of the lines in the spectrum than does the Gaussian model, according to the Monte Carlo simulations of the distribution of C statistic values. The goodness of fit values (expressed as a percentage of the Monte Carlo simulations that gave a C statistic as good as or better than that derived from the fit to the actual data; lower percentages are better) are listed in Table 4. All the wind-profile fits are formally good.

We calculated errors on the derived model parameters by using a three-dimensional grid of models in the parameter space of interest (q - $R_{\rm min}$ - τ_*) and applying a ΔC criterion appropriate for jointly-distributed uncertainties for three parameters ($\Delta C = 3.53$ for three parameters of interest), and reporting the maximum extent of this confidence region in each

of the three parameters as the formal uncertainties on the derived parameters. These are the values listed in Table 4, and shown, for two particular fits, in Figure 5.

5. Discussion

We summarize the derived model parameters and their uncertainties for each line in Figure 6. This figure shows that there are no obvious trends in any of the wind-profile model parameters with wavelength (or any other characteristic) of the emission lines. Fitting a function linear in wavelength to the uncertainty-weighted model parameters shows consistency with a constant function for each of the three parameters. The fitting results shown in Figure 6 present a consistent picture of a line profile model with an onset radius, $R_{\rm min} \approx 1.5{\rm R}_*$, $q \approx 0$, and $\tau_* \approx 0.25$ to 0.5. These are all reasonable parameters in the context of the general instability-driven wind-shock model, though the τ_* values are small compared to the expectations of wind theory, which we elaborate on below. Finally, we note that several of the stronger lines cannot be well fit by models with no wind absorption ($\tau_* = 0$ is ruled out), which is consistent with the inability of Gaussian models to provide good fits and also with the non-zero third moments of the line profiles, as discussed earlier. Looking at the situation from a different point of view, upper limits on the wind absorption are above $\tau_* = 0.5$ for all but one line in the spectrum. The unmistakable conclusion is that the *Chandra* spectrum of ζ Ori is consistent with a moderate amount of wind absorption (as well as the expected degree of broadening from an embedded wind source), and that at least some wind attenuation is demanded by the data.

The derived $R_{\rm min}$ and q values are consistent with the numerical simulations of the line-force instability wind shocks, inferred from simulation output shown in various figures in Cooper (1996); Cohen et al. (1996); Feldmeier et al. (1997); Owocki & Runacres (2002). These trends are also qualitatively understood from a theoretical point of view. The strong, relatively symmetric diffuse (scattered) radiation field near the photosphere inhibits the line-force instability and thus the formation of strong shocks near the photosphere, and the filling factor is not strongly dependent on radius because although the propensity of shocks to form eventually falls off with distance from the photosphere, the cooling timescale for shock-heated plasma increases with distance.

Given the spatial distribution of hot plasma derived from the line-profile fits, the continuum attenuation by the overlying cool wind is governed by the mass-loss rate and wind opacity. In the model we have employed, the overall wind attenuation is characterized by the optical depth parameter, $\tau_* \equiv \frac{\kappa \dot{M}}{4\pi v_\infty {\rm R}_*}$. Using mean values from Table 1 and a wind opacity value of $\kappa \approx 200$ cm^2 g^{-1}, we expect $\tau_* \approx 5$. The value for the wind opacity is taken from

Fig. 4 in Cohen et al. (1996). Of all the values that go into this calculation, the mass-loss rate is probably the most uncertain, followed by the wind opacity and the star's radius. The terminal velocity is probably known to within ten or twenty percent (which is the range of values found in the literature).

Thus, the value of the wind optical depth parameterized by τ_*, as derived from the observed X-ray line profiles, is about an order of magnitude lower than the expected value. This is similar to what is seen in ζ Pup (Kramer, Cohen, & Owocki 2003), where the observed value of τ_* is almost an order of magnitude lower than expected (there is also a fair amount of uncertainty in the relevant properties of ζ Pup). The expected τ_* value for ζ Pup is about a factor of two larger than that for ζ Ori, primarily because of the earlier type star's larger mass-loss rate.

The fact that the X-ray line profiles of ζ Pup, and now ζ Ori, indicate lower than expected wind optical depths is consistent with recent work that indicates that O star mass-loss rates may have been overestimated by a factor of three or more (Bouret, Lanz, & Hillier 2005) due to clumping (which affects density squared mass-loss diagnostics, such as radio free-free and H-alpha emission). This result is not inconsistent with the traditional UV absorption-line based mass-loss rate estimates of hot-star winds, which have always been subject to uncertainty due to the difficulty of reliably accounting for ionization distribution effects.

Other work, focusing on far-UV absorption line studies of many O and B supergiants, indicates that mass-loss rates may be overestimated by as much as an order of magnitude (Fullerton, Massa, & Prinja 2004). Clumping itself, even apart from its effect on mass-loss rate estimates, has the potential to reduce the mean opacity of a stellar wind (Feldmeier, Oskinova, & Hamman 2003; Oskinova, Feldmeier, & Hamman 2004). This effect might more accurately be termed "porosity" as it is the existence of a low density interclump region that potentially allows photons to escape the wind more easily (Owocki, Gayley, & Shaviv 2004). Feldmeier, Oskinova, & Hamman (2003); Oskinova, Feldmeier, & Hamman (2004) have shown significant effects on theoretical X-ray line profiles due to clumping (especially when the clumps are non-spherical; flattened and oriented parallel to the photosphere). However, these authors' work also predicts unusual line profile shapes that aren't seen in the *Chandra* data. And furthermore, for clumping/porosity to be truly effective at reducing the overall wind optical depth, individual clumps must be optically thick, and the "porosity length," which is the ratio of the typical clump size to the clump volume filling factor, must be large. In Appendix A we explore the requirements for clumping and porosity to reduce the mean wind optical depth and show that for the wind of ζ Ori, this would require clumping on a scale that is not expected from the wind instability mechanism, either in terms of the clump

filling factor or the typical clump separation.

The results from our X-ray emission line profile analysis should be consistent with other aspects of the *Chandra* observations. The emission measure and temperature information derived from the observations (Waldron & Cassinelli 2001) are typical for O supergiants and do not provide any significant constraints on the interpretation of the line profiles, aside from simply being broadly consistent with the expectations of the standard wind-shock scenario. The lack of significant X-ray time variability is also typical of hot stars and is usually taken to imply that the sites of shock heating in the wind are so numerous that despite the relatively rapid evolution of any one shock front, the global average over the entire wind of all the shock-heated regions is relatively constant.

By far the most constraining specific X-ray diagnostic in conjunction with the emission line profiles is the forbidden-to-intercombination emission line ratio in the helium-like isoelectronic sequence (Gabriel & Jordan 1969; Blumenthal, Drake, & Tucker 1972). In the presence of a strong UV field which can drive photoexcitation of electrons from the upper level of the forbidden line to the upper level of the intercombination line (2s $^3S_1$ - 2p $^3P_{1,2}$) and thus reduce the f/i line ratio, it can be used as a diagnostic of the UV mean intensity and thus of the distance of the X-ray emitting plasma from the photosphere.

The initial work on the several helium-like f/i ratios seen in the *Chandra* spectra from ζ Ori showed that most of the helium-like ions were far from the photosphere, consistent with those ions being embedded in the stellar wind, but that the Si XIII f/i ratio implied a location only slightly above the photosphere, which would generally be considered too close to the star to be consistent with any wind-shock scenario (Waldron & Cassinelli 2001). However, a recent reanalysis of these same data showed that all the helium like ions, including Si XIII, are consistent with an onset radius ($R_{\rm min}$) of about 1.5R$_*$ (Leutenegger et al. 2006). This result is, of course, completely consistent with those we report here for the emission line profiles of eleven other lines in the *Chandra* data.

We can also consider trends in the derived wind profile parameters within our dataset. One might expect different lines to have different morphologies and thus different model parameters either because different ions form at different temperatures and thus sample different shocked regions or because lines at different wavelengths have differing amounts of wind attenuation due to the wavelength dependence of the opacity of the bulk, cold wind. Photoionization cross sections of cosmically abundant plasma do have a strong wavelength dependence over a large range of wavelengths. However, this effect is more complex when the plasma is ionized, as it is even in the "cold" component of a hot-star wind. Furthermore, the lines we analyze in this paper span only a factor of two in wavelength. Looking at the wind opacity in Fig. 4 of Cohen et al. (1996), we can see that the values of the wind opacity

range only over about a factor of 2 from 600 eV (roughly the photon energy of the O VII lines near 21 Å which are the longest-wavelength lines to which we fit the wind profile model) to 1000 eV (roughly the photon energy of the Ne X Ly_α line, which is the shortest wavelength line we discuss here). The variations in the wind opacity on this relatively small wavelength range are complex and not monotonic, because of the dominance of photoionization edges of oxygen (O^{+3} through O^{+5}). The appearance of these edges breaks up the usual E^{-3} fall off in opacity, and over this relatively small wavelength range, makes the opacity roughly constant. If anything, the longest wavelength lines in our data (the O VII lines near 21 Å) are subject to less attenuation than the shorter wavelength lines, by virtue of their being longward of the oxygen K-shell edges (and, in fact, this emission feature has the lowest upper limit to the τ_* parameter of any of the lines we fit). In any case, there are no statistically significant trends in any of the three wind profile model parameters. As we discussed above, a single value of each parameter is consistent with all the data. So, although higher signal-to-noise data in the future may reveal a significant trend, none is seen in these data.

Finally, we note that each line or line complex is well fit, in a statistical sense, by the relatively simple, spherically symmetric wind-profile model we employ here. Future higher resolution and/or higher signal-to-noise spectra could show evidence for signatures of wind asymmetry or of time variability in the line profiles (perhaps much like DACs see in UV absorption lines from the winds of hot stars or like moving emission bumps seen in WR spectra). There is, however, no need at this point to invoke either of these effects nor any others that go beyond the very basic model we have used here.

6. Conclusions

The fundamental observational conclusions of this work are that the X-ray emission lines of the late O supergiant ζ Ori are broad, blue shifted, and modestly asymmetric, which is qualitatively consistent with the general picture of hot, X-ray emitting plasma embedded in an expanding, spherically symmetric stellar wind. These results come both from fitting a physics-based empirical wind-profile model to eleven emission lines in the *Chandra* MEG spectrum, and also from attempts to fit Gaussian line-profile models and a non-parametric analysis of the line shapes via the calculation of the first three moments of eight unblended lines.

There is no need, based on the observed line profiles, to invoke ad hoc coronal emission or other non-standard or unphysical X-ray production mechanisms. However, the amount of attenuation by the bulk, cold stellar wind is significantly less than would be expected by a simple application of the assumed mass-loss rate, standard warm plasma opacities,

and the assumption of a spherically symmetric, smooth stellar wind. Qualitatively, this result is consistent with the results of a similar analysis of the *Chandra* spectrum of the early O star, ζ Pup (Kramer, Cohen, & Owocki 2003). And the smaller-than-expected wind attenuation leaves an observational signature that explains why previous studies, in which Gaussian profiles were fit and then analyzed "by eye," did not identify the signature of wind attenuation. The emission lines, though significantly blue shifted, are only modestly asymmetric, and in fact, any individual line can be at least marginally well fit by a blue shifted Gaussian. In the aggregate, however, there is a significant improvement in the fits based on the wind-profile models as compared to those based on Gaussians.

These results, taken together with the earlier ones on the X-ray line profiles of ζ Pup, indicate then that the standard wind-shock scenario is adequate for explaining the high-resolution X-ray spectra for normal O supergiants. Unusual hot stars, such as γ Cas, θ^1 Ori C, and τ Sco, do not fit into this paradigm, perhaps because of their extreme youth (especially in the case of the last two of these), but there is no reason, especially now that the helium-like f/i line ratios have also been reanalyzed (Leutenegger et al. 2006), to suppose that all hot stars, with the sole exception of ζ Pup, pose an insurmountable challenge to the wind-shock model of X-ray production. That being said, the wind-shock model still has various difficulties in accounting in detail for the observed trends in X-ray properties among OB stars, and there are many open questions about the specific ingredients of a correct wind-shock model. But the nature of X-ray emission line profiles in O supergiants, while providing some interesting constraints and presenting a puzzle about wind optical depths, does not require us to completely discard the wind-shock paradigm or lead us to invoke coronal models for explaining hot-star X-ray emission. The lower than expected wind optical depths derived from the X-ray line profiles do, however, add to the debate about O star mass-loss rates and the role of wind clumping.

We wish to thank J. Elliot Reed for initial work with the *Mathematica* modeling code and the moment analysis. DHC acknowledges NASA contract NAS8-03060, to Swarthmore College through the Chandra X-ray Center. SPO acknowledges NSF grants AST-0097983 and AST-0507581. RHK acknowledges NASA grant yyy (Joe's LTSA) to Prism Computational Sciences, and also the support of the Howard Hughes Medical Institute grant to Swarthmore College. DHC and KG thank the National Science Foundation for its support to the Keck Northeast Astronomy Consortium through grant AST-0353997.

REFERENCES

Babel, J. & Montmerle, T. 1997a, A&A, 323, 121

Babel, J. & Montmerle, T. 1997b, ApJ, 485, L29

Berghofer, T. W. & Schmitt, J. H. M. M. 1994, *Science*, 265, 1689

Blumenthal, G. R., Drake, G. W. F. & Tucker, W. H. 1972, ApJ, 172, 205

Bouret, J.-C., Lanz, T., & Hillier, D. J. 2005, A&A, 438, 301

Cash, W. 1979, ApJ, 228, 939

Cassinelli, J. P., Cohen, D. H., MacFarlane, J. J., Sanders, W. T., & Welsh, B. Y. 1994, ApJ, 421, 705

Cassinelli, J. P., Miller, N. A., Waldron, W. L., MacFarlane, J. J., & Cohen, D. H. 2001, ApJ, 554, L55

Cassinelli, J. P., & Olson, G. L. 1979, ApJ, 229, 304

Chen, W., & White, R. L. 1991, ApJ, 366, 512

Cohen, D. H., Cooper, R. G., MacFarlane, J. J, Owocki, S. P., Cassinelli, J. P. & Wang, P. 1996, ApJ, 460, 506

Cohen, D. H., de Messières, G. E., MacFarlane, J. J., Miller, N. A., Cassinelli, J. P., Owocki, S. P., & Liedahl, D. A. 2003, ApJ, 586, 495

Cooper, R. G. 1996, Ph.D. thesis, University of Delaware

Corcoran, M. F., et al. 1993, ApJ, 412, 792

Dessart, L. & Owocki, S. P. 2003, A&A, 406, L1

Drew, J. E., Hoare, M. G., & Denby, M. 1994, MNRAS, 266, 917

Feldmeier, A., Kudritzki, R.-P., Palsa, R., Pauldrach, A. W. A., & Puls, J. 1997a, A&A, 320, 899

Feldmeier, A., Oskinova, L., & Hamman, W.-R. 2003, A&A, 403, 217

Feldmeier, A., Puls, J., & Pauldrach, A. W. A. 1997b, A&A, 322, 878

Fullerton, A. W., Massa, D. L., & Prinja, R. K. 2004, *BAAS*, 205, 5304

Gabriel, A. H., & Jordan, C. 1969, MNRAS, 145, 241

Gagné, M., Caillault, J.-P., Stauffer, J. R., Linsky, J. L. 1997, ApJ, 478, L87

Gagné, M., Oksala, M., Cohen, D. H., Tonnesen, S. K., ud-Doula, A., Owocki, S. P., Townsend, R. H. D., & MacFarlane, J. J. 2005, ApJ, 628, 986

Hillier, D. J., Kudritzki, R. P., Pauldrach, A. W., Baade, D., Cassinelli, J. P., Puls, J., & Schmitt, J. H. M. M. 1993, ApJ, 276, 117

Ignace, R. 2001, ApJ, 549, L119

Kahn, S. M., Leutenegger, M. A., Cottam, J., Rauw, G., Vreux, J.-M., den Boggende, A. J. F., Mewe, R., & Güdel, M. 2001, A&A, 365, L312

Kramer, R. H., Cohen, D. H., & Owocki, S. P. 2003, ApJ, 592, 532

Kramer, R. H., Tonnesen, S. K., Cohen, D. H., Owocki, S. P., ud-Doula, A., & MacFarlane, J. J. 2003, *Rev. Sci. Inst.*, 74, 1966

Kudritzki, R. P., Palsa, R., Feldmeier, A., Puls, J. & Pauldrach, A. W. A. 1996, in *Röntgenstrahlung from the Universe*, eds. H. U. Zimmermann, J. Trümper, & H. Yorke (Munich: MPE), 9

Leutenegger, M., Paerels, F., Kahn, S., & Cohen, D. H. 2006, in preparation

Lucy, L. B. 1982, ApJ, 255, 286

Lucy, L. B., & Solomon, P. M. 1970, ApJ, 159, 879

Lucy, L. B., & White, R. L. 1980, ApJ, 241, 300

MacFarlane, J. J., & Cassinelli, J. P. 1989, ApJ, 347, 1090

MacFarlane, J. J., Cassinelli, J. P., Welsh, B. Y., Vedder, P. W., Vallerga, J. V., & Waldron, W. L. 1991, ApJ, 380, 564

Maíz-Apellániz, J., Walborn, N. R., Galué, H. Á., & Wei, L. H. 2004, ApJS, 151, 103

Mewe, R., Raassen, A. J. J., Cassinelli, J. P., van der Hucht, K. A., Miller, N. A., & Güdel, M. 2003, A&A, 398, 203

Miller, N. A., Cassinelli, J. P., Waldron, W. L., MacFarlane, J. J., & Cohen, D. H. 2002, ApJ, 577, 951

Mullan, D. J. 1984, ApJ, 283, 303

Oskinova, L., Feldmeier, A., & Hamman, W.-R. 2004, A&A, 422, 675

Owocki, S. P., Castor, J. I., & Rybicki, G. B. 1988, ApJ, 335, 914

Owocki, S. P., & Cohen, D. H. 1999, ApJ, 520, 833

Owocki, S. P. & Cohen, D. H. 2001, ApJ, 559, 1108

Owocki, S. P., Gayley, K. G. & Shaviv, N. J. 2004, ApJ, 616, 525

Owocki, S. P. & Runacres, M. C. 2002, A&A, 318, 1015

Owocki, S. P. & Rybicki, G. B. 1984, ApJ, 284, 337

Pallavicini, R., Golub, L., Rosner, R., Vaiana, G. S., Ayres, T., & Linsky, J. L. 1981, ApJ, 248, 279

Perryman, M. A. C., et al. 1997, A&A, 323, L49

Runacres, M. C. & Owocki, S. P. 2002, A&A, 381, 1015

Schulz, N. S., Canizares, C., Huenemoerder, D., & Tibbets, K. 2003, ApJ, 595, 365

Smith, M. A., Cohen, D. H., Gu, M. F., Robinson, R. D., Evans, N. R., & Schran, P. G. 2004, ApJ, 600, 972

Smith, M. A., Grady, C. A., Peters, G. J., & Feigelson, E. D. 1993, ApJ, 409, L49

ud-Doula, A.,& Owocki, S. P. 2002, ApJ, 576, 413

Waldron, W. L. 1984, ApJ, 282, 256

Waldron, W. L., & Cassinelli, J. P. 2001, ApJ, 548, L45

A. Optical Depth in a Porous Medium

Let us derive here some simple relations for how the absorption in a wind outflow could be affected by the "porosity" of the medium. We begin by writing the expression for radial optical depth in a smooth stellar wind,

$$\tau(r) = \int_r^\infty dr'\, \kappa\rho(r') = \frac{\kappa \dot{M}}{4\pi v_\infty R_*} \frac{\mathrm{R}_*}{\mathrm{r}} \equiv \tau_* \frac{\mathrm{R}_*}{\mathrm{r}} \equiv \frac{R_1}{r}\,, \tag{A1}$$

where for simplicity we've assumed a constant flow speed v_∞, and have defined the characteristic wind optical depth τ_* and the unit optical depth radius $R_1 = \tau_* \mathrm{R}_*$ in terms of the mass loss rate $\dot{M}$ and stellar radius R_*.

Following the discussion in §5 of (Owocki, Gayley, & Shaviv 2004) (see particularly their eqn. 35), consider then a porous wind in which the microscopic opacity is modified into an "effective opacity",

$$\kappa_{\rm eff} = \kappa \frac{1-e^{-\tau_{\rm b}}}{\tau_{\rm b}} \tag{A2}$$

$$\approx \kappa \quad ; \quad \tau_{\rm b} \ll 1 \tag{A3}$$

$$\approx \frac{\kappa}{\tau_{\rm b}} = \frac{\ell^2}{m_{\rm b}} = \frac{1}{\rho H} \; ; \quad \tau_{\rm b} \gg 1\,, \tag{A4}$$

where $\tau_{\rm b} = \kappa\rho H$ is the optical depth of individual clumps or blobs, with $H = \ell/f$ the "porosity length" for clumps of scale ℓ and volume filling factor f. The last equality shows that optically thick blobs have an effective opacity given by the ratio of their area ℓ^2 to mass $m_{\rm b} (= \ell^3\rho/f = \ell^2\rho H)$.

Application of (A4) into (A1) gives

$$\tau_{\rm eff}(r) = \int_r^\infty dr' \kappa_{\rm eff}(r')\rho(r') \tag{A5}$$

$$\approx \frac{R_1}{r} \quad ; \quad r \geq R_{\rm b} \tag{A6}$$

$$\approx \frac{R_{\rm b} - r}{H} + \frac{R_1}{R_{\rm b}} \; ; \quad r \leq R_{\rm b}\,, \tag{A7}$$

where the radius at which $\tau_{\rm b} = 1$ is given by $R_{\rm b} = \sqrt{HR_1}$. We thus see that the radius $R_{\rm b1}$ at which $\tau_{\rm eff}(R_{\rm b1}) \equiv 1$ is given by

$$R_{\rm b1} \approx R_1 \quad ; \quad R_{\rm b} \leq R_1 \tag{A8}$$

$$\approx 2R_{\rm b} - H = R_{\rm b}(2 - R_{\rm b}/R_1) \; ; \quad R_{\rm b} \geq R_1\,. \tag{A9}$$

Then defining $h \equiv \sqrt{H/R_1}$ $(= H/R_{\rm b} = R_{\rm b}/R_1)$, the reduction in the radius of unit optical depth can be written[1]

$$\frac{R_{\rm b1}}{R_1} = h(2-h) \quad ; \quad 1 \le h \le 2\,, \tag{A10}$$

A central result here is that a reduction in the unit optial depth radius (which is what is required to make the wind more transparent) requires $h > 1$. That is, it requires a quite large porosity length, larger than the unit optical depth radius in the smooth wind, i.e. $H > R_1$. Since $H \equiv \ell/f$, this requires either very large blobs, $\ell \gtrsim R_1$, or very small filling factors, $f < \ell/R_1$, or some combination of these.

In this regard, we note that structure arising from the line-driven instability has a typical spatial scale on the order of the mean-wind Sobolov length, $L \equiv v_{\rm th}/(dv/dr) \approx (v_{\rm th}/v_\infty)\mathrm{R}_* \approx \mathrm{R}_*/100$, and a typical volume filling factor of order $f \gtrsim 1/10$. This implies an associated porosity length $H \lesssim \mathrm{R}_*/10$, about a factor 100 too small to reduce the absorption for a typical optically thick case with $\tau_* \approx 10$, and thus $R_1 \approx 10\mathrm{R}_*$.

It thus seems rather unlikely that the structure arising from the line-driven instability could lead to a substantial porosity that allows the wind to be more transparent to absorption of, e.g. X-rays. If porosity is a contributing factor in the apparent reduced absorption of such X-rays, it requires structure on a relatively large spatial scale, or a very small volume filling factor.

Another key general point here is that the "porosity" effect in reducing absorption is quite distinct from the "clumping" effect that can enhance processes that scale with density-squared. The latter depends only on the volume filling factor f, while the former depends on this filling factor *and* the characteristic spatial scale of the structure, in the combination characterized by the porosity length $H = \ell/f$. This distinction stems from the fact that the porosity effect requires the individual blobs or clumps to be optically thick, so that material in the front side of the blob can effectively "hide" or "shadow" other material within the blob, thus reducing the overall effective opacity of the medium.

Such a requirement makes porosity more effective in "inside-out" radiative transport, such as in reducing the effective coupling between radiative and matter in a stellar envelope and atmosphere. As shown in Owocki, Gayley, & Shaviv (2004) this can, for example, allow a super-Eddington star to have a quasi-steady wind from a bound surface. In contrast, it

[1]The potential reduction of the radius $R_{\rm b1}$ to zero is a consequence of the simplifying assumptions of a constant expanding medium consisting purely of clumps, without any smooth "interclump" material. More realistically, the minimum of the unit optical depth radius would be set by the static stellar radius, i.e. $R_{\rm b1} > \mathrm{R}_*$.

seems inherently more difficult for porosity to play a role in "outside-in" problems, such as the transparency of wind X-ray emission as viewed by an external observer, which is the case of principal concern in this paper.

Table 1. Stellar Properties of ζ Orionis from Various Authors

Reference	M ($M_\odot$)	R ($R_\odot$)	M_v	$B-V$	$\dot{M}/10^{-6}$ ($M_\odot$ yr^{-1})	v_∞ (km s^{-1})
Lamers and Leitherer (1993)	49	31	-7.0	—	2.51	2100
Prinja et al. (1991)	—	—	—	—	—	1860
Blomme (1990)	(37)	—	-6.7	—	—	2400
Groenewegen et al. (1989)	41	26	-6.6	—	—	2100
Voels et al. (1989)	34	24	—	-0.27	—	—
Wilson and Dopita (1985)	25	20	—	—	1.58	2190

Table 2. Gaussian Line Profile Fits to the Emission Lines

Ion	λ_o (Å)	Centroid (km s^{-1})	HWHM (km s^{-1})
N VII	24.781	-110 ± 140	1380^{+140}_{-130}
O VIII	18.969	-150 ± 30	830^{+30}_{-20}
O VII	18.627	-390 ± 70	530^{+100}_{-80}
Fe XVII	16.787	-350 ± 50	900 ± 50
O VIII	16.006	-180 ± 60	840 ± 60
Fe XVII	15.261	-450 ± 120	1660^{+140}_{-120}
Fe XVII	15.014	-210 ± 40	780^{+40}_{-30}
Ne X	12.134	-200 ± 40	870 ± 40
Ne IX	11.544	-390 ± 140	1360^{+160}_{-150}

Table 3. First and Third Moments of the Emission Line Profiles

Ion	λ_o (Å)	M1	M1/uncert.	M3	M3/uncert.
O VIII	18.969	-0.0818 ± 0.0135	-6.08	7.9914 ± 4.8511	1.65
O VII	18.627	-0.1138 ± 0.0416	-2.74	4.5943 ± 2.9983	1.53
Fe XVII	16.787	-0.1652 ± 0.0229	-7.32	7.5967 ± 3.9259	1.94
O VIII	16.006	-0.0464 ± 0.0247	-1.88	3.9309 ± 3.8114	1.03
Fe XVII	15.261	-0.1371 ± 0.0313	-4.38	11.0659 ± 5.5266	2.00
Fe XVII	15.014	-0.0792 ± 0.0173	-4.58	12.5198 ± 5.5363	2.26
Ne X	12.134	$-0.0801 \pm .0194$	-4.13	10.1529 ± 5.4936	1.85
Ne IX	11.544	-0.1108 ± 0.0368	-3.01	2.8778 ± 4.0377	0.71

Table 4. Wind Profile Model Parameters Fit to the Data

Ion	λ_o (Å)	q	$R_{\rm min}/R_*$	τ_*	Goodness of fit[a]
O VII	21.8036, 21.6015	$-0.25^{+.39}_{-.25}$	$1.66^{+.19}_{-.15}$	$0.06^{+.17}_{-.06}$	0.38
O VIII	18.9689	$-0.12^{+.35}_{-.26}$	$1.60^{+.19}_{-0.13}$	$0.26^{+.23}_{-.16}$	0.68
O VII	18.627	$0.48^{+2.22}_{-.88}$	$1.30^{+.37}_{-.22}$	$1.35^{+2.32}_{-.88}$	0.58
Fe XVII	17.051, 17.096	$0.28^{+1.82}_{-.88}$	$1.07^{+2.70}_{-1.06}$	$4.63^{+2.84}_{-4.34}$	0.51
Fe XVIII	16.780	$-0.05^{+unc.}_{-.65}$	$2.26^{+2.44}_{-1.25}$	$0.70^{+1.81}_{-.59}$	0.87
O VIII	16.006	$-0.30^{+unc.}_{-.37}$	$1.52^{+1.43}_{-0.28}$	$0.27^{+.56}_{-.27}$	0.57
Fe XVII	15.261	$0.28^{+unc.}_{-.35}$	$1.02^{+2.33}_{-.01}$	$4.68^{+unc}_{-4.15}$	0.54
Fe XVII	15.014	$-0.39^{+.33}_{-.20}$	$1.38^{+.20}_{-0.17}$	$0.58^{+.49}_{-.31}$	0.32
Ne X	12.134	$-0.48^{+.48}_{-.21}$	$1.50^{+.27}_{-.15}$	$0.07^{+.45}_{-.07}$	0.63

[a]Fraction of Monte Carlo simulated datasets that gave a C statistic as good or better than that given by the best-fit model and the data. This can be interpreted as a rejection probability.

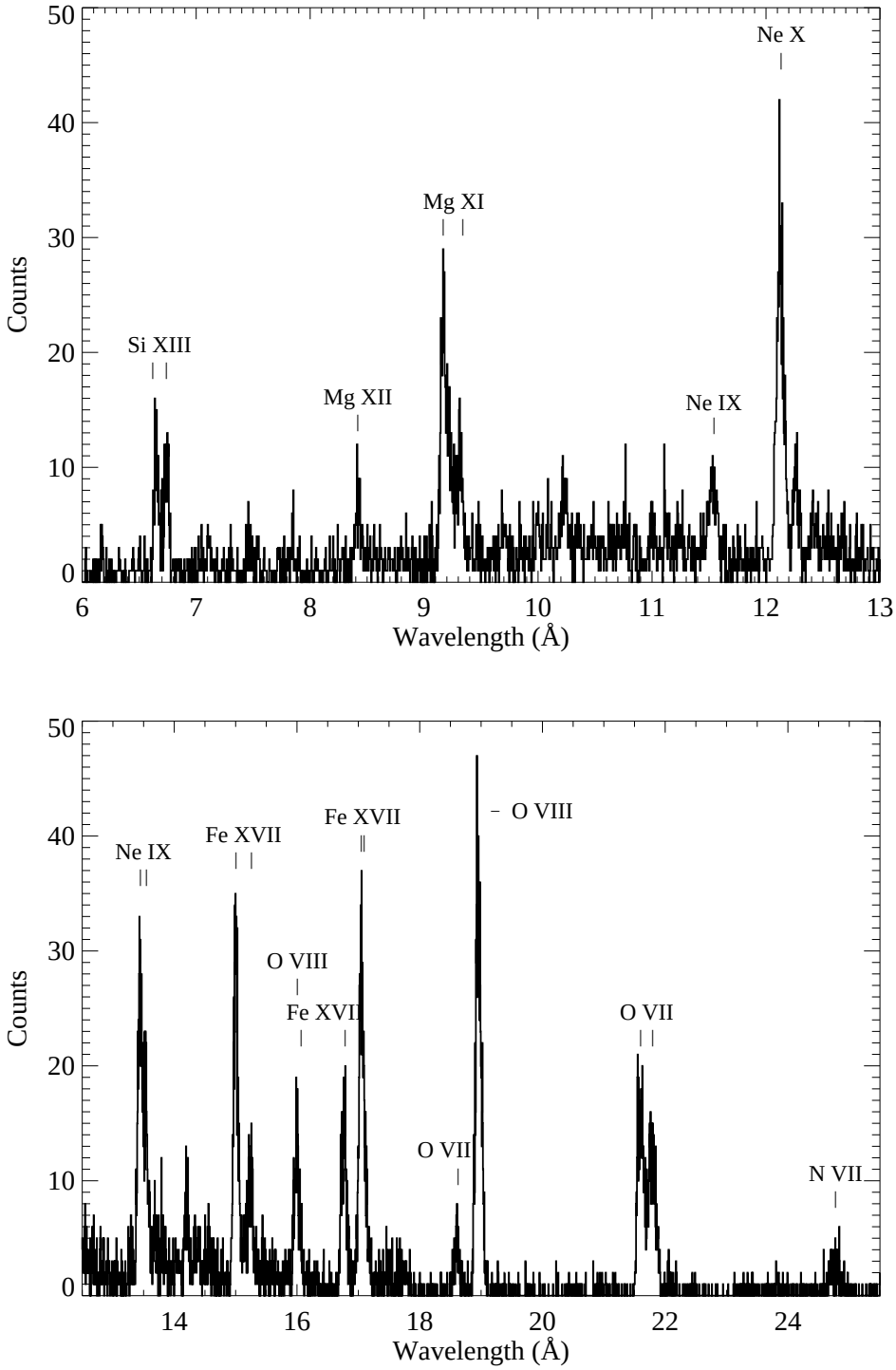

Fig. 1.— The MEG spectrum of ζ Ori, with negative and positive first orders from both observations (Obs. IDs 610 and 1524) coadded.

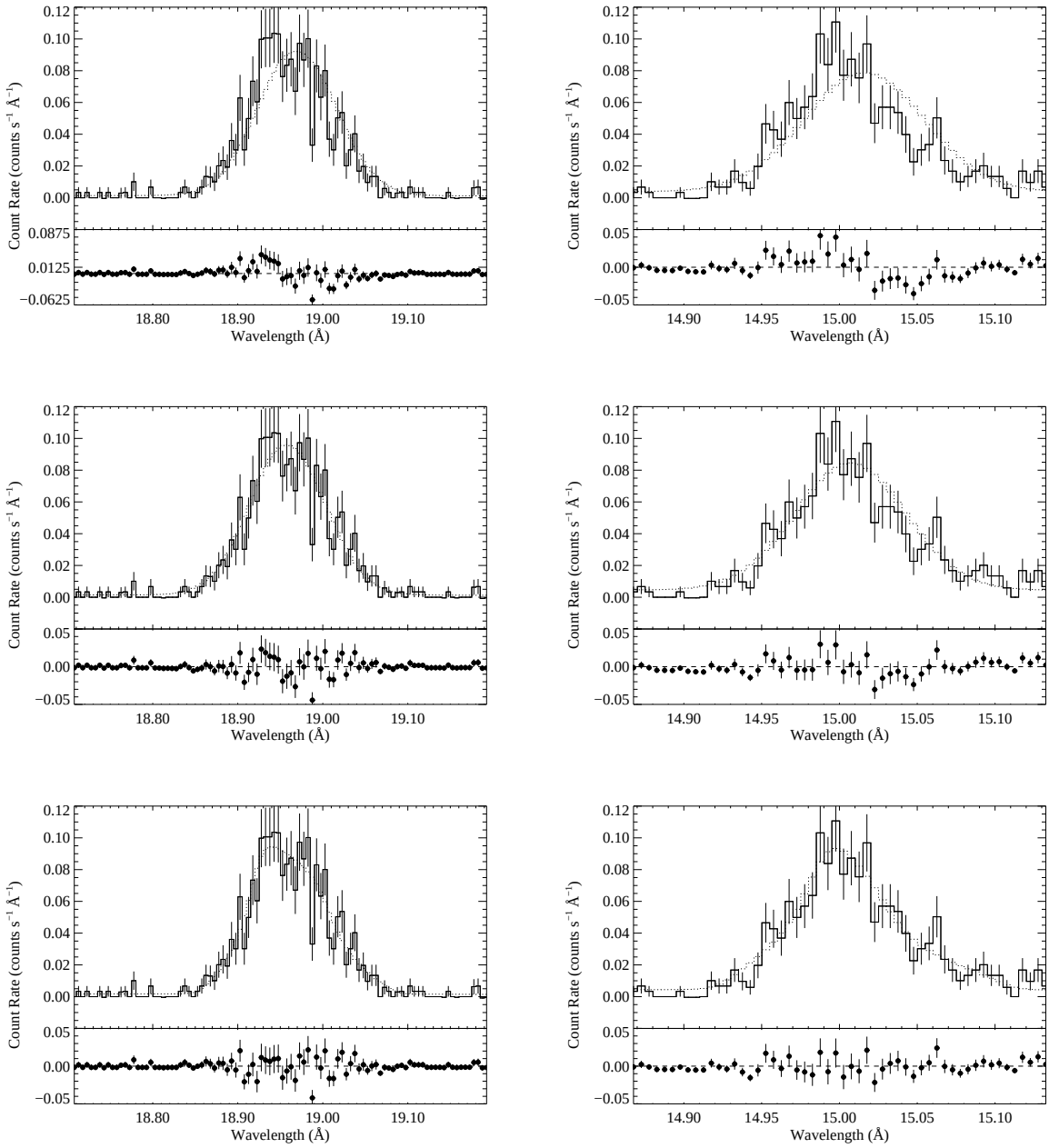

Fig. 2.— Best-fit models superimposed on the observed O VIII Ly_α line (left-hand column) and the Fe XVII 15.014 Å line (right-hand column). The fit shown in the top row is for a Gaussian model with the line center fixed at the laboratory rest wavelength. This fits shown in the middle row are for the Gaussian model with the centroid treated as a free parameter. The Gaussian fits in the first two rows are discussed in Sec. 3. The fits shown in the lower panel are for the wind-profile model discussed in Sec. 4.

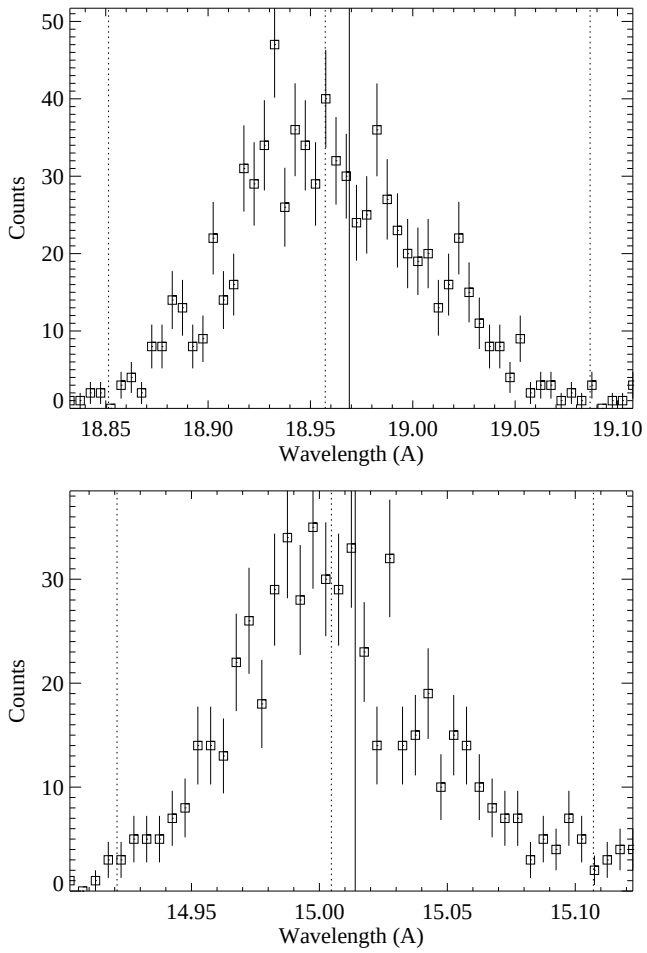

Fig. 3.— The same two representative emission lines shown in Figure 2, with their centroids as determined from the moment analysis. O VIII Lyman-alpha at 18.97 Å (top) has a centroid (first moment) 6 sigma from the laboratory rest wavelength, and a positive third moment (red skewed) that is significant at the 1.7 sigma level. The Fe XVII line at 15.01 Å (bottom) has a significantly negative first moment (5 sigma) and a third moment that is positive at the 2.3 sigma level (see Table 3). In both panels, the solid vertical line is the laboratory rest wavelength, while the dashed line to its immediate left represents the first moment. The other two dashed lines represent the blue and red limits over which the moment analysis was performed ($x = -1, 1$).

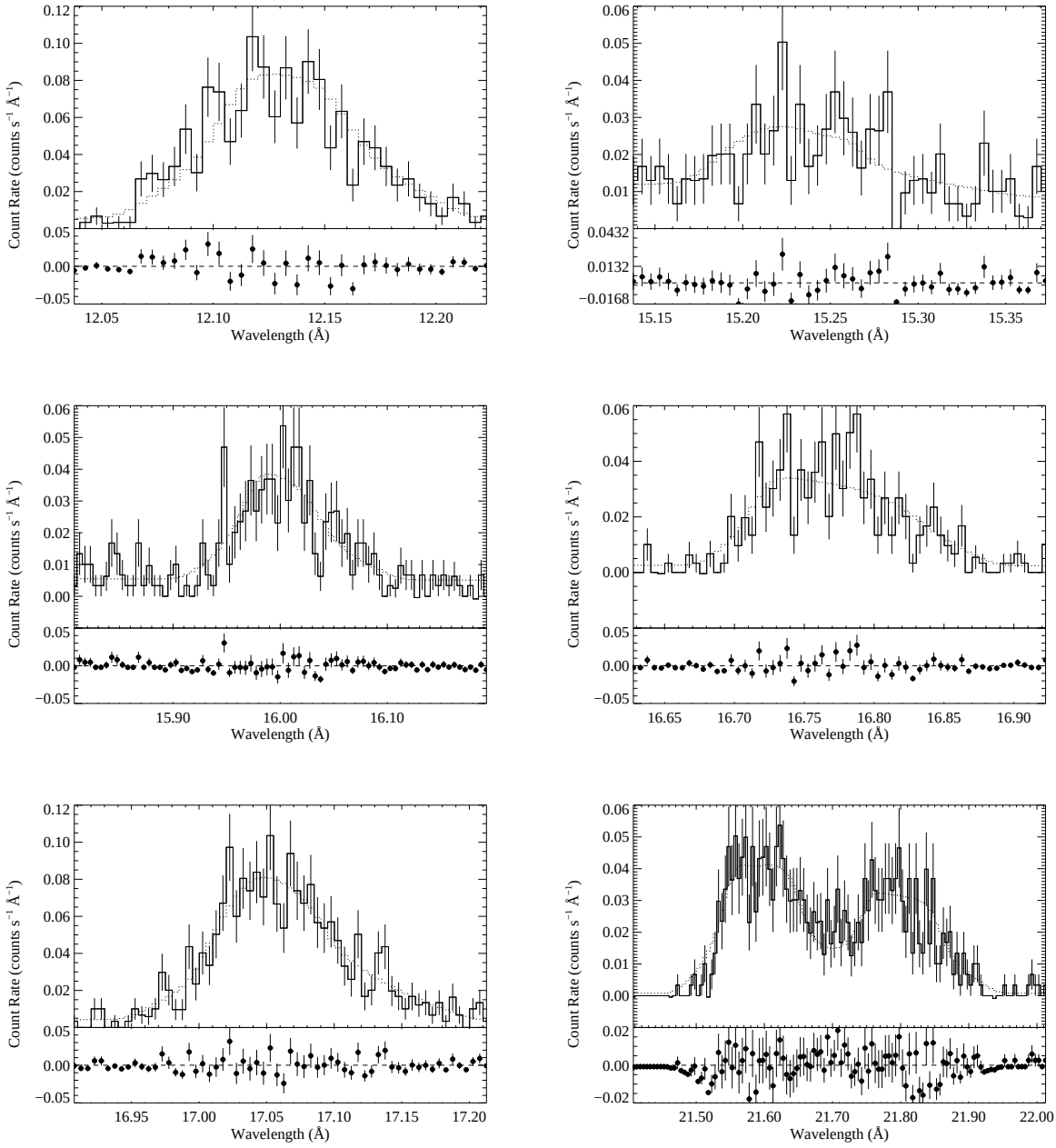

Fig. 4.— Best-fit wind-profile models for six additional lines (or line complexes): Ne X 12.13 Å, Fe XVII 15.26 Å, O VII 16.01 Å, Fe XVII 17.051 Å and 17.096 Å, O VII 18.627 Å, and O VII 21.60 Å and 21.80 Å.

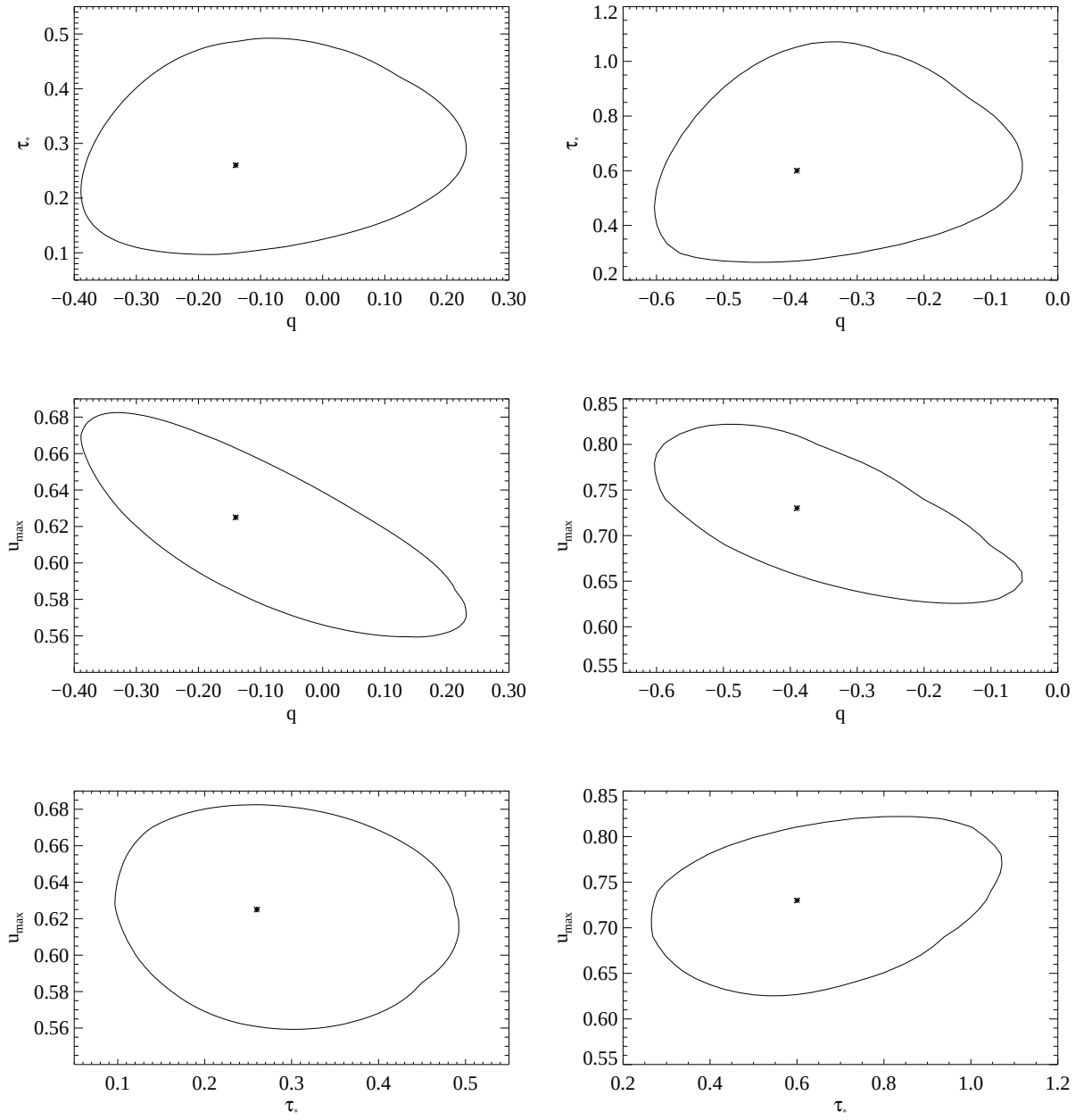

Fig. 5.— Projections of the confidence regions in the parameter space of the wind-profile model, for the two lines shown in Figure 2, the O VIII Ly$_\alpha$ line (left-hand column) and the Fe XVII 15.01 Å line (right-hand column). Note the correlation between q and $R_{\rm min}$ ($u_{\rm max}^{-1}$).

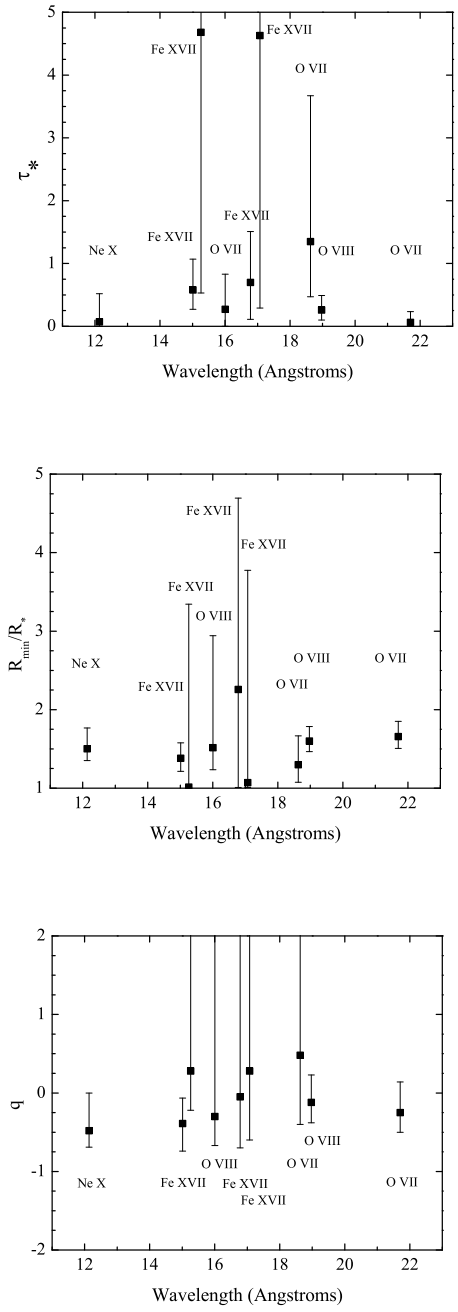

Fig. 6.— The best-fit model parameters - τ_*, R_{min}, and q - for each line we fit with a wind-profile model. The extent of the 68% confidence regions for the joint probability distribution of the three parameters ($\Delta C = 3.53$; the extent of the contours shown in Fig. 5, projected onto the relevant axes) are indicated by error bars.